Dynamical Generation of Topological Magnetic Lattices for Ultracold Atoms

Jinlong Yu, Zhi-Fang Xu, Rong Lü, and Li You

Dynamical generation of topological magnetic lattices for ultracold atoms

Jinlong Yu,[1,3] Zhi-Fang Xu,[2,3,*] Rong Lü,[1,4] and L. You[1,4]

[1]*State Key Laboratory of Low Dimensional Quantum Physics,*
Department of Physics, Tsinghua University, Beijing 100084, China
[2]*MOE Key Laboratory of Fundamental Physical Quantities Measurements,*
School of Physics, Huazhong University of Science and Technology, Wuhan 430074, China
[3]*Department of Physics and Astronomy, University of Pittsburgh, Pittsburgh, Pennsylvania 15260, USA*
[4]*Collaborative Innovation Center of Quantum Matter, Beijing 100084, China*

We propose a scheme to dynamically synthesize a space-periodic effective magnetic field for neutral atoms by time-periodic magnetic field pulses. When atomic spin adiabatically follows the direction of the effective magnetic field, an adiabatic scalar potential together with a geometric vector potential emerges for the atomic center-of-mass motion, due to the Berry phase effect. While atoms hop between honeycomb lattice sites formed by the minima of the adiabatic potential, complex Peierls phase factors in the hopping coefficients are induced by the vector potential, which facilitate a topological Chern insulator. With further tuning of external parameters, both topological phase transition and topological flat band can be achieved, highlighting realistic prospects for studying strongly correlated phenomena in this system. Our work presents an alternative pathway towards creating and manipulating topological states of ultracold atoms by magnetic fields.

Gauge fields lay at the center of our modern understanding of physics in systems ranging from high energy to condensed matter and to ultracold atoms. Within this paradigm, interactions between particles, which enable rich quantum phases of a many-body system, are mediated through gauge fields. For instance, solid state materials with charged quasi-particles in magnetic fields or with spin-orbit coupling (SOC) show a rich variety of quantum Hall effect and exotic topological superconductivity [1, 2]. The interplay between gauge fields and lattice systems is also of great interests [3]. The spectrum of a charged particle in a square lattice exposed to a strong uniform magnetic field shows a fractal structure, widely known as the Hofstadter butterfly [4]. In another seminal work, Haldane shows that quantum Hall effect without Landau levels can be realized when a periodically staggered magnetic field is applied to charged particles in a honeycomb lattice [5].

Ultracold atoms in lattice systems are considered powerful simulators for studying gauge field physics [6–23]. Both the Hofstadter and the Haldane model with cold atoms were theoretically proposed [11–14] and experimentally demonstrated [15–21] by making use of novel forms of light-atom interactions [7], such as laser assisted tunneling [15–18], shaking-optical-lattice technique [21] and SOC within a synthetic dimension [19, 20]. In addition to the optical lattice formed from space-periodic ac-Stark shift by interfering laser beams, the ideas of generating a magnetic lattice with space-periodic Zeeman shift are also proposed [24–32] (and some realized [25–28]), using current-carrying wires [24], microfabricated wires or permanent magnetic structures on atomic chips [25–30], superconducting vortex lattice shields [31], as well as phase imprinting by gradient magnetic pulses [32]. In contrast to optical lattices, magnetic lattices are free from atomic spontaneous emissions that are always accompanied by heating and loss of atoms. Additionally, they have the potential to reach shorter lattice constants [30, 31] (of a few tens

of nanometers as proposed in Ref. [31]), leading to improved energy scales and less stringent temperature requirements; the lattice constants can even be continuously tuned [32]. These advantageous features enhance the performance of atomic quantum gases as powerful quantum simulators.

While the simulation of gauge field physics and manipulation of topological states in optical lattices have shown fruitful results [6–23], it remains to show whether this is also the case for magnetic lattices. This work provides an affirmative first answer to this question.

This Letter presents a scheme for synthesizing a time independent effective Hamiltonian with non-trivial band topology for atomic gases with internal spin degrees of freedom, based on the phase imprinting technique [33, 34]. A two-dimensional (2D) magnetic lattice with triangular geometry emerges in the effective Hamiltonian. In the limit when an atom is confined in the lowest Zeeman level, an adiabatic scalar potential and a geometric vector potential are simultaneously generated for the center-of-mass motion [6, 22, 23]. The adiabatic scalar potential surface can form a honeycomb lattice, while the associated geometric vector potential provides complex phases for next nearest neighbor (NNN) hopping coefficients in realizing the Haldane model [5, 35]. With the flexibility and tunability of magnetic fields, our scheme can be extended to produce a set of effective Hamiltonians, whose lowest energy bands undertake a topological phase transition from a topological (Chern) insulator to a trivial one. Moreover, models possessing topological quasi-flat bands are realized near the phase transition point.

The protocol.—We consider a pancake shaped quasi-2D ultracold atomic gas of spin-F confined in the x-y plane (at $z = 0$). In the presence of a bias magnetic field $B_0\hat{e}_z$, the single-particle Hamiltonian is given by

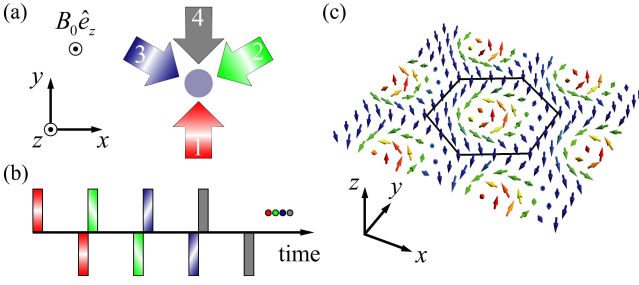$$H_0 = \frac{\mathbf{p}^2}{2m} + \hbar\omega_0 F_z, \tag{1}$$

FIG. 1. (Color online) A schematic illustration for synthesizing a magnetic lattice. (a) An atomic cloud is exposed to a uniform bias magnetic field $B_0\hat{e}_z$ (pointing out of the page), and subjected in sequence to four pairs of opposite magnetic pulses as shown in (b). Pulse pairs 1, 2 and 3 are gradient magnetic fields lying in the x-y plane along directions separated by 120°. Pulse pair 4 executes $\mp\pi$ spin rotations along the y-direction. The color gradient represents the corresponding magnetic field strength. (b) The time-periodic pulse sequence with four pairs of pulses forms one complete evolution period. (c) A three-dimensional view of the effective magnetic field $\mathbf{B}_{\text{eff}}$ [Eq. (5)], which forms a Skyrmion lattice [39] with its Wigner-Seitz unit cell shown by the hexagon [of edge length $4\pi/(3k_{\text{so}})$]. The arrows are colored by the magnitude of the third component of $\mathbf{B}_{\text{eff}}$.

where $\mathbf{p} = (p_x, p_y)$ is the 2D kinetic momentum, m is the atomic mass, $\hbar$ is the reduced Planck constant, F_z is the third component of the atomic spin vector (in unit of $\hbar$) $\mathbf{F} = (F_x, F_y, F_z)$ and $\omega_0 = g_F \mu_B B_0/\hbar$ is the Larmor frequency at B_0, where g_F is the Landé g-factor for the spin-F hyperfine state manifold and μ_B is the Bohr magneton.

A short gradient magnetic field pulse $B'y\hat{e}_y$ of duration $\delta t'$ imprints a space-dependent phase factor [32–34, 36–38] onto the wavefunction as $\exp\left(-ik_{\text{so}}yF_y\right)$, where $k_{\text{so}} = \delta t' g_F \mu_B B'/\hbar$ is the SOC strength [36, 37] with B' the magnetic gradient. After a free evolution time δt, a second magnetic field pulse in the opposite direction imprints an opposite phase. The two pulses combined together enact a unitary transformation

$$e^{ik_{\text{so}}yF_y} F_z e^{-ik_{\text{so}}yF_y} = F_z \cos(k_{\text{so}}y) - F_x \sin(k_{\text{so}}y), \quad (2)$$

which rotates the magnetic field $B_0 (0, 0, 1)$ to a space-periodic form $B_0(-\sin(k_{\text{so}}y), 0, \cos(k_{\text{so}}y))$. Similarly, an opposite uniform field pulse pair $\mp B_y\hat{e}_y$ with a pulse area $\delta t' g_F \mu_B B_y/\hbar = \pi$ inverts the magnetic field $B_0 (0, 0, 1)$ to $B_0 (0, 0, -1)$ as $e^{-i\pi F_y} F_z e^{i\pi F_y} = -F_z$. More generally, a gradient magnetic field pulse along an arbitrary direction $\hat{e}_\theta = (\cos\theta, \sin\theta, 0)$ in the x-y plane imprints a phase factor $\exp(-ik_{\text{so}}r_\theta F_\theta)$, where $r_\theta = \mathbf{r} \cdot \hat{e}_\theta = x\cos\theta + y\sin\theta$ and $F_\theta = \mathbf{F} \cdot \hat{e}_\theta = F_x \cos\theta + F_y \sin\theta$ are respectively the coordinate vector $\mathbf{r} = (x, y)$ and the spin vector $\mathbf{F}$ projected to the $\hat{e}_\theta$ direction. Following a period of free evolution and a second pulse from an opposite gradient field, an expression analogous to Eq. (2) generates a magnetic field with spatial periodicity along the $\hat{e}_\theta$ direction.

In our scheme to be discussed below, repeated pulse pairs are concatenated. A complete cycle of the evolution period contains three gradient pulse pairs along directions separated by an angle of 120°, together with a $\mp\pi$ pulse pair along y-direction as shown in Fig. 1(a-b). The total evolution over one

complete cycle (of period $T = 4\delta t$) is then given by

$$U(T,0) = e^{-i\pi F_y} e^{-iH_0\delta t/\hbar} e^{i\pi F_y}$$
$$\times \prod_{j=3,2,1} e^{ik_{\text{so}}r_{\theta_j}F_{\theta_j}} e^{-iH_0\delta t/\hbar} e^{-ik_{\text{so}}r_{\theta_j}F_{\theta_j}}, \quad (3)$$

with $\theta_j = -\frac{\pi}{6} + \frac{2\pi j}{3}$. According to the Floquet theorem [40, 41], a time-independent effective Hamiltonian can be defined according to $U(T,0) \equiv \exp(-iH_{\text{eff}}T/\hbar)$. To the lowest order of T, we find [42]

$$H_{\text{eff}} = \frac{1}{2m}\left(\mathbf{p} - \frac{3}{8}\hbar k_{\text{so}}\mathbf{F}_\perp\right)^2 + \frac{15}{64}\hbar\omega_{\text{so}}\mathbf{F}_\perp^2 + g_F\mu_B\mathbf{B}_{\text{eff}} \cdot \mathbf{F}, \quad (4)$$

where $\mathbf{F}_\perp = (F_x, F_y)$ is the 2D spin operator, $\omega_{\text{so}} = \hbar k_{\text{so}}^2/2m$ is the SOC frequency, and $\mathbf{B}_{\text{eff}}$ is an effective magnetic field whose three components are given by

$$B_{\text{eff},x} = -\frac{B_0}{4}\sum_j \sin\left(k_{\text{so}}r_{\theta_j}\right)\sin\theta_j,$$
$$B_{\text{eff},y} = \frac{B_0}{4}\sum_j \sin\left(k_{\text{so}}r_{\theta_j}\right)\cos\theta_j, \quad (5)$$
$$B_{\text{eff},z} = \frac{B_0}{4}\left[-1 + \sum_j \cos\left(k_{\text{so}}r_{\theta_j}\right)\right].$$

The first two terms in Eq. (4) arise from the unitary transformations by gradient pulse pairs applied to the momentum operator [32, 36]. The third term describes a magnetic (Zeeman) lattice that couples the atomic spin to the effective magnetic field $\mathbf{B}_{\text{eff}}$, as shown in Fig. 1(c).

Geometric potentials and energy spectrum.—The above protocol for the generation of a triangular magnetic lattice is general, and can be applied to atoms with arbitrary spins. For concreteness, we choose a specific atomic species, fermionic ^{6}Li, with electron spin $J = 1/2$, nuclear spin $I = 1$, and consider the total hyperfine spin $F = I - J = 1/2$ ground state manifold. The Landé g-factor can be evaluated according to the Breit-Rabi formula [43] to be $g_F \approx -1/3$. The spin operator reduces to $\mathbf{F} = \boldsymbol{\sigma}/2$, where $\boldsymbol{\sigma}$ is the vector of Pauli matrices. To be more specific, in all numerical calculations, we assume a set of fixed parameters unless otherwise noted. They are $B_0 = 20$ mG, $B'\delta t' = 2$ G cm^{-1} ms [44], which correspond to $k_{\text{so}} = (1.7\,\mu\text{m})^{-1}$ and $\omega_0 = 32.3\omega_{\text{so}} = (2\pi) \times 9.3$ kHz for the $F = 1/2$ manifold of ^{6}Li. With these parameters, the lattice term in Eq. (4) dominates during time evolution.

We denote the space-dependent eigenstates of the magnetic lattice by $|\chi_{1,2}(\mathbf{r})\rangle$ which satisfy,

$$g_F\mu_B\mathbf{B}_{\text{eff}} \cdot \frac{\boldsymbol{\sigma}}{2}|\chi_{1,2}(\mathbf{r})\rangle = \pm\epsilon_0(\mathbf{r})|\chi_{1,2}(\mathbf{r})\rangle, \quad (6)$$

where $\epsilon_0(\mathbf{r}) = -|g_F\mu_B\mathbf{B}_{\text{eff}}|/2$ is the adiabatic potential for atomic center-of-mass motion in the lower energy eigenstate $|\chi_1\rangle$. For an atom adiabatically moving in this space-periodic Zeeman level, a vector potential $\mathbf{A}(\mathbf{r})$ emerges [42, 45],

$$\mathbf{A} = i\hbar\langle\chi_1|\nabla\chi_1\rangle + \frac{3}{16}\hbar k_{\text{so}}\langle\chi_1|\boldsymbol{\sigma}_\perp|\chi_1\rangle, \quad (7)$$

with $\boldsymbol{\sigma}_\perp = (\sigma_x, \sigma_y)$. Associated with the vector potential is the flux density $n_\phi = (\nabla \times \mathbf{A})_z/2\pi\hbar$, which shares the same
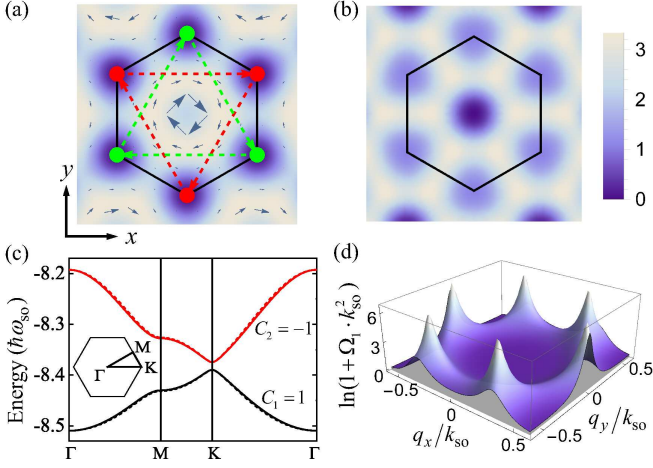
FIG. 2. (Color online) Mapping the effective Hamiltonian [Eq. (4)] to the Haldane model. (a) The density plot of the adiabatic potential ϵ_0 (in blue color) and its associated vector potential $\mathbf{A}$ shown by field of arrows. Darker color denotes smaller ϵ_0, and the minima of which form a honeycomb lattice, with two sites per unit cell, respectively denoted by red and green filled circles. The dashed lines denote NNN hopping paths along directions of positive Peierls phases. (b) The flux density n_ϕ, in unit of $10^{-2}k_{so}^2$. The hexagons in (a) and (b) denote the primitive unit cell [the same as in Fig. 1(c)], over which the net flux is unity. (c) Energy spectrum. *Solid lines*: the lowest two energy bands along lines with high symmetry in the first Brillouin zone (inserted hexagon) for the effective Hamiltonian Eq. (4), with $\omega_0 = 32.3\omega_{so}$. *Dashed lines*: fitted band structure using the Haldane model results. The edge length of the inserted hexagon is $k_{so}/\sqrt{3}$. (d) A logarithmic plot of the Berry curvature for the lowest band Ω_1. The integration of Ω_1 in the first Brillouin zone gives its Chern number $C_1 = 1$.

spatial periodicity as $\mathbf{B}_{eff}$ and can be considered as a type of flux lattice [22] in general.

The adiabatic potential ϵ_0, vector potential $\mathbf{A}$, and the flux density n_ϕ for our magnetic lattice are shown in Fig. 2(a) and (b) [46]. As shown in Fig. 2(a), the local minima of ϵ_0 are located at the corners of the unit cell, forming a honeycomb lattice. When an atom hops between these honeycomb sites, the vector potential contributes a complex Peierls phase factor $\exp\left(i\int \mathbf{A}\cdot d\mathbf{l}/\hbar\right)$ to the hopping coefficient [4, 5, 35], with the integration evaluated along the corresponding hopping path. As $\mathbf{A}$ vanishes along the edges of the hexagon, the nearest-neighboring (NN) phase factor is a trivial unity. While along the NNN hopping paths [dashed lines in Fig. 2(a)], the accumulated phases are always non-zero. Thus the adiabatic scalar potential together with the geometric vector potential realizes the Haldane model in the tight-binding limit. As a caveat, our flux pattern shown in Fig. 2(b) is not the same as suggested by Haldane [5], where the staggered flux density gives a vanishing net flux over a unit cell. The flux distribution shown in Fig. 2(b) is non-negative everywhere, and the net flux over one unit cell is unity rather than zero, which can be checked by integrating over a unit cell the following: $N_\phi = \frac{1}{4\pi}\int_{UC} dx\,dy\,\left(\mathbf{m}\cdot\partial_x\mathbf{m}\times\partial_y\mathbf{m}\right)$, with $\mathbf{m} = \mathbf{B}_{eff}/|\mathbf{B}_{eff}|$ [22].

Thus the non-trivial winding pattern of $\mathbf{B}_{eff}$ shown in Fig. 1(c) leads to a quantized net flux $N_\phi = 1$. A non-zero net flux generally leads to larger Peierls phases (of order unity). It also promises simulation of charged particles in strong magnetic field with non-dispersive Landau levels [22, 47].

To quantitatively confirm our model indeed maps onto the Haldane model, we numerically study the spectrum and Berry curvature [48] of the effective Hamiltonian Eq. (4) using the plane wave expansion method [42, 49]. The typical band structure and the Berry curvature for the lowest band are shown respectively in Fig. 2(c) and (d). A band gap opens at the corners of the first Brillouin zone ($\pm K$ points), where the Berry curvature is maximum. Both the eigenenergies and the Berry curvatures are even functions of quasi-momentum, so the spectrum at $K' = -K$ is not shown. The Chern numbers [50] for the lowest two bands are $C_{1,2} = \pm 1$ respectively. The spectrum and the Berry curvature thus resemble the ones from the Haldane model. To further validate this correspondence, we adopt the method used in Ref. [51] to get the NN hopping constant t_1 and the complex NNN hopping constant $|t_2|e^{i\phi}$ of the Haldane model from the calculated band structure. We find $t_1 = 0.053\hbar\omega_{so}$ and $|t_2| = 0.0037\hbar\omega_{so}$ with $\phi = 0.40$. Using these three parameters together with an overall energy shift, the tight-binding band structure of the Haldane model is plotted as the dashed lines in Fig. 2(c).

Topological phase transition and quasi-flat bands.—Our protocol allows for easy tuning of two parameters: the SOC strength $k_{so} = \delta t' g_F \mu_B B'/\hbar$, and the bias magnetic field B_0. Both can be tuned continuously, and can be turned on adiabatically to reach the ground state for our model system Eq. (4) [8, 21] (see [42] for details). Once the ground state is achieved, we can apply an additional weak optical gradient field (which commutes with all the pulse manipulation operations) in the x-y plane to drive Bloch oscillations and then measure the perpendicular center-of-mass drift to extract the topological properties for the lowest energy band [17, 21, 52]. With unequal durations between subsequent pulse pairs, or allowing for specific k_{so} and B_0 values for different subperiods, several variants of the effective Hamiltonian can be synthesized. A topological phase transition for the lowest energy band can be achieved by a simple tuning of the bias magnetic field. For this to occur, we set the field strength to be B_0 for the first three subperiods and switch to αB_0 for the fourth subperiod, our protocol then leads to a change for the z-component of the effective magnetic field in Eq. (5) as

$$B_{eff,z} = \frac{B_0}{4}\left[-\alpha + \sum_j \cos\left(k_{so}r_{\theta_j}\right)\right]. \tag{8}$$

The $\alpha = 1$ case corresponds to the original proposal with topological bands, while the $\alpha = 0$ case describes a system of trivial energy bands with zero Chern numbers. By continuously tuning α from 0 to 1, a topological phase transition with band touching and re-opening takes place, as summarized in Fig. 3.

Figure 3(a) presents the changing Chern number, hence the band topology, for the lowest band with increasing α. The lattice geometry of the adiabatic potential is found to undergo
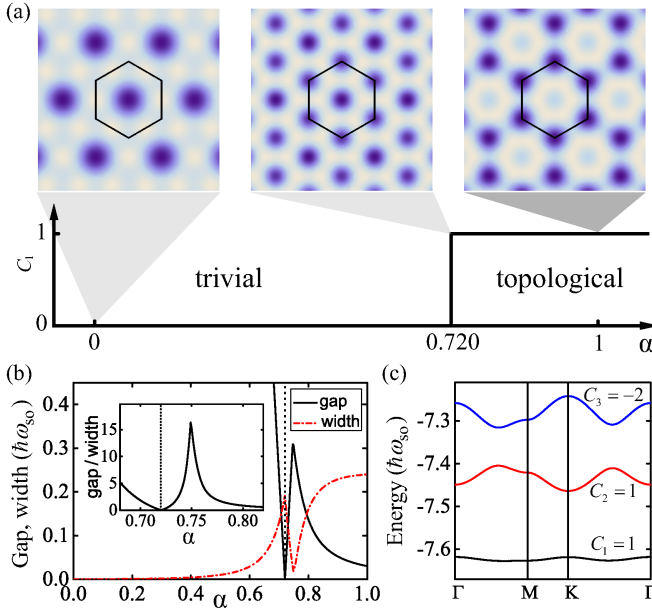
FIG. 3. (Color online) Illustration of the structural and topological phase transition with tuning of the z-component of $\mathbf{B}_{\text{eff}}$ in Eq. (8). (a) Top panel: the density plots of the adiabatic potentials for $\alpha = 0$ (left), $\alpha = 0.720$ (middle), and $\alpha = 1$ (right) with the minima (dark colors) forming simple triangular lattice, decorated triangular lattice, and honeycomb lattice respectively. Bottom panel: The Chern number for the lowest energy band as a function of α. A topological phase transition occurs at the critical point of $\alpha = 0.720$. (b) The band gap between the lowest two bands and the band width for the lowest band, as a function of α. The band gap closes at $\alpha = 0.720$ (marked by the dotted vertical line). The inset shows the dependence of band gap-over-width ratio on α. It is peaked at $\alpha = 0.749$ with a value 16. (c) The lowest three bands at $\alpha = 0.749$.

a structural transformation from a simple triangular lattice, to a decorated triangular lattice [53], and finally to a honeycomb lattice. The corresponding tight-binding descriptions for s-orbitals involve 1, 3, and 2 bands respectively for the three cases. As α increases, the band originating from hopping between s-orbitals located at unit cell centers crosses the two bands from s-orbitals located at the corners. Their corresponding Chern numbers change after band touching and reopening. Figure 3(b) shows the behavior of the gap between the lowest two bands as well as the band width for the lowest one. Gap closing occurs at Γ point when $\alpha = 0.720$, and the gap-over-width ratio is found to be quite large over a limited range after gap opening with a peak value as large as 16 when $\alpha = 0.749$, as shown in the inset of Fig. 3(b). The energy spectrum at $\alpha = 0.749$ is shown in Fig. 3(c). The lowest band is a Landau-level–like topological quasi-flat one [54]. Such a non-dispersive topological band also persists beyond the adiabatic limit [42]. It is a promising candidate for simulating fractional quantum Hall effect when suitable interactions are included [55–58]. It is perhaps worthy pointing out that, flat band can emerge as the second excited band in a Kagome lattice [53], or as the first excited band in a Lieb lattice [59].

The properties of the localized states in the flat band of a Lieb lattice have been investigated in a recent experiment [59].

In this work, we focus on discussing single-particle physics of a fermionic spin-1/2 system, although our magnetic lattice generation protocol can be equally applied to a higher spin atom, be it a boson or fermion. When local momentum-independent (s-wave) interaction is taken into account, it can be simply added to the effective Hamiltonian because it commutes with all the pulse manipulation operations (see also [36, 37]). The topological phase is expected to be stable to weak interactions due to the presence of a gap. However stronger interaction can drive the system to new phases, in which the physics may be dominated by the interplay between correlation and band topology. A detailed study of the interaction effects for this system deserves further efforts.

In conclusion, we propose an experimentally feasible protocol to realize a synthetic magnetic field with real magnetic field pulses. The synthetic magnetic field forms a lattice with non-trivial band topology, and under certain limits can be mapped to the Haldane model. The high tunability of our scheme makes it possible to design a topological phase transition as well as quasi-flat energy bands with non-trivial topology, which can push the effective model into the strongly correlated regime.

* zfxu83@hust.edu.cn
[1] M. Z. Hasan and C. L. Kane, Rev. Mod. Phys. 82, 3045 (2010).
[2] X.-L. Qi and S.-C. Zhang, Rev. Mod. Phys. 83, 1057 (2011).
[3] For a pedagogical review, see B. A. Bernevig and T. L. Hughes, Topological Insulators and Topological Superconductors (Princeton University Press, Princeton, 2013).
[4] D. R. Hofstadter, Phys. Rev. B 14, 2239 (1976).
[5] F. D. M. Haldane, Phys. Rev. Lett. 61, 2015 (1988).
[6] J. Dalibard, F. Gerbier, G. Juzeliūnas, and P. Öhberg, Rev. Mod. Phys. 83, 1523 (2011).
[7] N. Goldman, G. Juzeliūnas, P. Öhberg, and I. B. Spielman, Rep. Prog. Phys. 77, 126401 (2014).
[8] N. Goldman and J. Dalibard, Phys. Rev. X 4, 031027 (2014).
[9] J. Struck, C. Ölschläger, R. Le Targat, P. Soltan-Panahi, A. Eckardt, M. Lewenstein, P. Windpassinger, and K. Sengstock, Science 333, 996 (2011).
[10] P. Hauke, O. Tieleman, A. Celi, C. Ölschläger, J. Simonet, J. Struck, M. Weinberg, P. Windpassinger, K. Sengstock, M. Lewenstein, and A. Eckardt, Phys. Rev. Lett. 109, 145301 (2012).
[11] D. Jaksch and P. Zoller, New J. Phys. 5, 56 (2003).
[12] A. Celi, P. Massignan, J. Ruseckas, N. Goldman, I. B. Spielman, G. Juzeliūnas, and M. Lewenstein, Phys. Rev. Lett. 112, 043001 (2014).

[13] A. G. Grushin, A. Gómez-León, and T. Neupert, Phys. Rev. Lett. **112**, 156801 (2014).

[14] W. Zheng and H. Zhai, Phys. Rev. A **89**, 061603 (2014).

[15] M. Aidelsburger, M. Atala, M. Lohse, J. T. Barreiro, B. Paredes, and I. Bloch, Phys. Rev. Lett. **111**, 185301 (2013).

[16] H. Miyake, G. A. Siviloglou, C. J. Kennedy, W. C. Burton, and W. Ketterle, Phys. Rev. Lett. **111**, 185302 (2013).

[17] M. Aidelsburger, M. Lohse, C. Schweizer, M. Atala, J. T. Barreiro, S. Nascimbene, N. R. Cooper, I. Bloch, and N. Goldman, Nat Phys **11**, 162 (2015).

[18] C. J. Kennedy, W. C. Burton, W. C. Chung, and W. Ketterle, arXiv:1503.08243.

[19] M. Mancini, G. Pagano, G. Cappellini, L. Livi, M. Rider, J. Catani, C. Sias, P. Zoller, M. Inguscio, M. Dalmonte, and L. Fallani, Science **349**, 1510 (2015).

[20] B. K. Stuhl, H.-I. Lu, L. M. Aycock, D. Genkina, and I. B. Spielman, Science **349**, 1514 (2015).

[21] G. Jotzu, M. Messer, R. Desbuquois, M. Lebrat, T. Uehlinger, D. Greif, and T. Esslinger, Nature **515**, 237 (2014).

[22] N. R. Cooper, Phys. Rev. Lett. **106**, 175301 (2011).

[23] K. Jimenez-Garcia, L. J. LeBlanc, R. A. Williams, M. C. Beeler, A. R. Perry, and I. B. Spielman, Phys. Rev. Lett. **108**, 225303 (2012).

[24] J. Yin, W. Gao, J. Hu, and Y. Wang, Opt. Commun. **206**, 99 (2002).

[25] A. Günther, S. Kraft, M. Kemmler, D. Koelle, R. Kleiner, C. Zimmermann, and J. Fortágh, Phys. Rev. Lett. **95**, 170405 (2005).

[26] M. Singh, M. Volk, A. Akulshin, A. Sidorov, R. McLean, and P. Hannaford, J. Phys. B **41**, 065301 (2008).

[27] S. Whitlock, R. Gerritsma, T. Fernholz, and R. J. C. Spreeuw, New J. Phys. **11**, 023021 (2009).

[28] S. Jose, P. Surendran, Y. Wang, I. Herrera, L. Krzemien, S. Whitlock, R. McLean, A. Sidorov, and P. Hannaford, Phys. Rev. A **89**, 051602 (2014).

[29] A. Grabowski and T. Pfau, Euro. Phys. J. D **22**, 347 (2003).

[30] V. Leung, A. Tauschinsky, N. van Druten, and R. Spreeuw, Quantum Inf. Process. **10**, 955 (2011).

[31] O. Romero-Isart, C. Navau, A. Sanchez, P. Zoller, and J. I. Cirac, Phys. Rev. Lett. **111**, 145304 (2013).

[32] X. Luo, L. Wu, J. Chen, R. Lu, R. Wang, and L. You, New J. Phys. **17**, 083048 (2015).

[33] S. Burger, K. Bongs, S. Dettmer, W. Ertmer, K. Sengstock, A. Sanpera, G. V. Shlyapnikov, and M. Lewenstein, Phys. Rev. Lett. **83**, 5198 (1999).

[34] J. Denschlag, J. E. Simsarian, D. L. Feder, C. W. Clark, L. A. Collins, J. Cubizolles, L. Deng, E. W. Hagley, K. Helmerson, W. P. Reinhardt, S. L. Rolston, B. I. Schneider, and W. D. Phillips, Science **287**, 97 (2000).

[35] L. B. Shao, S.-L. Zhu, L. Sheng, D. Y. Xing, and Z. D. Wang, Phys. Rev. Lett. **101**, 246810 (2008).

[36] Z.-F. Xu, L. You, and M. Ueda, Phys. Rev. A **87**, 063634 (2013).

[37] B. M. Anderson, I. B. Spielman, and G. Juzeliūnas, Phys. Rev. Lett. **111**, 125301 (2013).

[38] X. Luo, L. Wu, J. Chen, Q. Guan, K. Gao, Z.-F. Xu, L. You, and R. Wang, arXiv:1502.07091.

[39] N. Nagaosa and Y. Tokura, Nat Nano **8**, 899 (2013).

[40] M. M. Maricq, Phys. Rev. B **25**, 6622 (1982).

[41] C. P. Slichter, *Principles of Magnetic Resonance*, 3rd ed. (Springer-Verlag, New York, 1990).

[42] See supplemental material for details on the derivation of effective Hamiltonian, the numerical methods employed for the energy spectrum and Berry curvature, the validity of the effective Hamiltonian, the reduction of the artificial gauge fields, the energy spectrum beyond the limit of adiabatic approximation, and the adiabatic preparation of the ground state.

[43] G. K. Woodgate, *Elementary Atomic Structure*, 2nd ed. (Oxford University Press, Oxford, 1980).

[44] A magnetic gradient pulse with B' as large as $400\,\mathrm{kG\,cm^{-1}}$ and duration $\delta t'$ less than $1\mu s$ is achivable in the state-of-the-art atomic chip experiments; see for example S. Machluf, Y. Japha, and R. Folman, Nat Commun **4**, 2424 (2013).

[45] A geometric scalar potential $W(\mathbf{r})$ also emerges along with the vector potential, whose contribution to the total scalar potential is negligibly small compared to the adiabatic potential in the adiabatic limit [42].

[46] The vector potential $\mathbf{A}$ contains a gauge dependent singularity, which is chosen to be at the center of the unit cell for the guage we use.

[47] N. R. Cooper and J. Dalibard, EPL **95**, 66004 (2011).

[48] D. Xiao, M.-C. Chang, and Q. Niu, Rev. Mod. Phys. **82**, 1959 (2010).

[49] N. W. Ashcroft and N. D. Mermin, *Solid State Physics* (Cengage Learning, 1976).

[50] D. J. Thouless, M. Kohmoto, M. P. Nightingale, and M. den Nijs, Phys. Rev. Lett. **49**, 405 (1982).

[51] J. Ibanez-Azpiroz, A. Eiguren, A. Bergara, G. Pettini, and M. Modugno, Phys. Rev. A **90**, 033609 (2014).

[52] A. Dauphin and N. Goldman, Phys. Rev. Lett. **111**, 135302 (2013).

[53] G.-B. Jo, J. Guzman, C. K. Thomas, P. Hosur, A. Vishwanath, and D. M. Stamper-Kurn, Phys. Rev. Lett. **108**, 045305 (2012).

[54] A. S. Sørensen, E. Demler, and M. D. Lukin, Phys. Rev. Lett. **94**, 086803 (2005).

[55] S. Yang, Z.-C. Gu, K. Sun, and S. Das Sarma, Phys. Rev. B **86**, 241112 (2012).

[56] S. A. Parameswaran, R. Roy, and S. L. Sondhi, C. R. Phys. **14**, 816 (2013).

[57] N. R. Cooper and J. Dalibard, Phys. Rev. Lett. **110**, 185301 (2013).

[58] E. J. Bergholtz and Z. Liu, Int. J. Mod. Phys. B **27**, 1330017 (2013).

[59] S. Taie, H. Ozawa, T. Ichinose, T. Nishio, S. Nakajima, and Y. Takahashi, arXiv:1506.00587.